Journal of Structural Geology, Vol. 15, No. 1, pp. 79 to 94, 1993
Printed in Great Britain

0191-8141/93 $06.00+0.00

High-amplitude folding of linear-viscous multilayers

KENNETH M. CRUIKSHANK* and ARVID M. JOHNSON

M. King Hubbert Structural Geology Laboratory, Earth and Atmospheric Sciences Department, Purdue University, 1397 CIVL Building, West Lafayette, IN 47907-1397, U.S.A.

(*Received* 5 *August* 1991; *accepted in revised form* 5 *May* 1992)

Abstract—High-amplitude folding of viscous multilayers during shortening can be analyzed with a theoretical solution motivated by first-order theoretical analysis of folding by Raymond Fletcher and Ronald Smith. The solution method can better match boundary conditions along irregular interfaces than the first-order method, so it increases the range of slopes over which linear-viscous folding theory can be applied. In our method, rather than solving algebraically for a small number of constants in the flow equations, we numerically solve for a large number of constants, the values of which are chosen so that they minimize errors in matching conditions at the interfaces in a least-squares sense. A similar method has been applied to problems of density instability involving a single deformable interface with bonded contacts; however, we extend the method to include shortening parallel to interfaces and many deformable interfaces so that we can deal with problems of multilayer folding. Contacts between the layers can be firmly bonded, slip freely, or slip with viscous resistance. We use the solution to produce high-amplitude folds in single layers embedded in soft media, and in simple repetitive multilayers confined above and below by stiff or soft media. We show that the folding of linear-viscous multilayers can largely reproduce the gross forms of some small folds in the Huasna syncline in the central California Coast Range as well as the Berry–Buffalo syncline in the central Pennsylvania Appalachians. However, the sharp, chevron-like forms in these natural examples are notably missing in the simulations based on linear-viscous theory.

INTRODUCTION

A THEORY of folding involving layers of viscous fluids has been developed independently for single-layer folds by Fletcher (1974, 1977) and Smith (1975), and further developed to analyze forms of folds in multilayers by Johnson & Pfaff (1989). The solutions are approximated, so that the analyses are limited to folding at low amplitudes. The basic analysis by Fletcher and Smith is to first order in the maximum slopes of interfaces. The analyses by Johnson & Pfaff (1989) are carried to third order but even these are probably limited to maximum limb slopes of less than 30°. The algebra becomes so complex that it has been infeasible to carry analyses to higher orders. Thus alternative solution methods are required to model high-amplitude folding. In this paper we describe a solution method, motivated by the basic theoretical developments by Fletcher (1967, 1977), for analyzing high-amplitude folding of a viscous multilayer during shortening. The method can match boundary conditions even along irregular interfaces, so it extends the range of slopes over which viscous-folding theory can be applied.

A similar solution method has been applied to problems of density instability involving a single deformable interface with bonded contacts by Fletcher (1967, 1972) and Nasir & Dabbousi (1978). We extend the method to include shortening parallel to interfaces and many deformable interfaces so that it can deal with problems of multilayer folding. Contacts between layers can be firmly bonded, slip freely, or slip with viscous resistance.

Almost all prior studies of high-amplitude folding have used finite-element methods (see review in Price & Cosgrove 1990), although other techniques such as variational methods have been tried (Chapple 1970). Perhaps the first attempt at high-amplitude folding using numerical methods was that by Dieterich & Onat (1969), who used a finite-element model to simulate a single interface undergoing shortening in order to produce mullion-like structures. The first use of finite-element models to analyze folding of a single stiff layer embedded in soft media was by Dieterich & Carter (1969), Dieterich (1970) and Parrish *et al.* (1976). Unfortunately, the models used a compressible material, and the results are not directly comparable with the results presented in this paper, although the final fold shapes are similar in many respects. Anthony & Wickham (1978) and Lan & Wang (1987) performed a finite-element analysis of single-layer folding, including the effect of layer-parallel shear. Lan & Hudleston (1991) have used finite-elements to investigate high-amplitude folding of a single layer of power-law material. deBremaecker & Becker (1978) used finite-elements to model the folding of a multilayer with three layers with bonded contacts.

The objective of this paper is to extend the basic theoretical analysis of multilayer folding by Johnson & Pfaff (1989) to higher amplitudes. We use their method for calculating the dominant and preferred wavelengths in a viscous multilayer, and use that information to provide a seed perturbation for the fold pattern. They use up to three terms plus all second- and third-order interactions in their exact solution. Our method leads to an approximate solution, but uses as many terms as are needed to adequately match conditions at boundaries. Thus the objective of this paper is to extend a rigorous

*Present address: Stanford Rock Fracture Project, Department of Applied Earth Sciences, Stanford University, Stanford, CA 94305-2225, U.S.A.

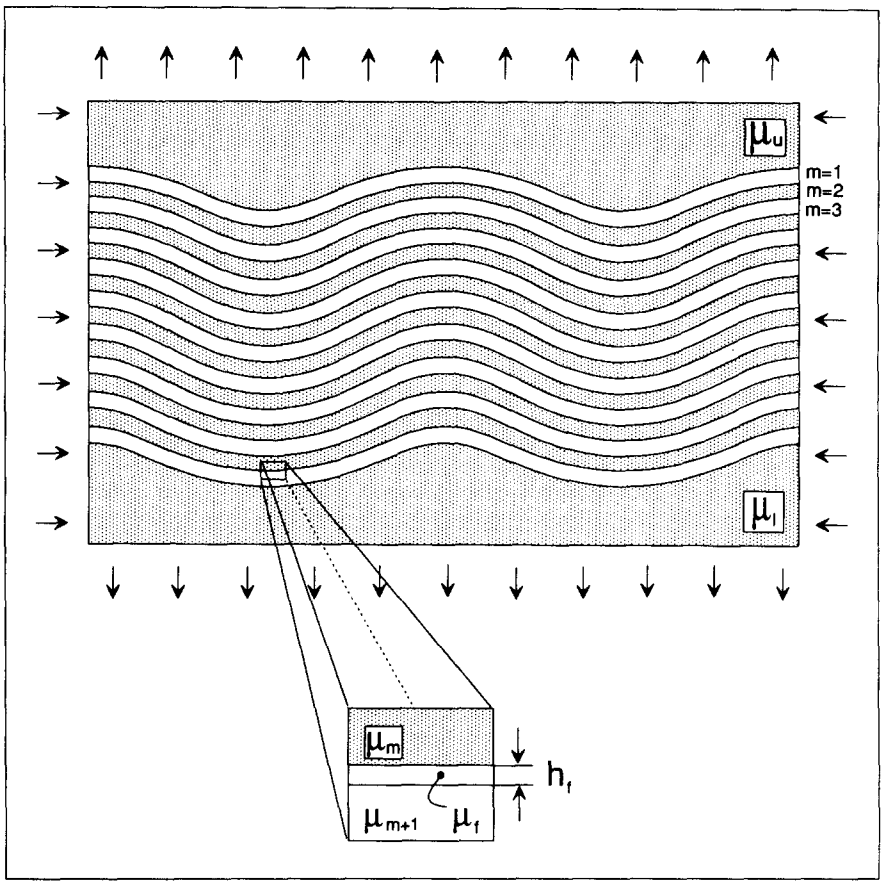

Fig. 1. In viscous folding theory a stratigraphic sequence is represented by layers of viscous fluids, subjected to layer-parallel shortening.

theory from moderate- to high-amplitude while maintaining the same boundary conditions and material properties.

The first part of this paper presents an outline of viscous-folding theory and the solution method. It then presents results of analyses for single layers and for simple repetitive multilayers. The fold forms in these idealized multilayers can be used to interpret mechanically more complicated multilayer systems. The final part of the paper uses the model to simulate some folds in the Huasna syncline in California (Johnson & Page 1976), and the Berry–Buffalo syncline in Pennsylvania (Aytuna 1984, Johnson & Pfaff 1989).

VISCOUS-FOLDING THEORY

Figure 1 shows the system that we wish to model. It is comprised of a stack of incompressible linear-viscous fluids embedded between infinite media. The system undergoes layer-parallel shortening, with accompanying layer-normal thickening. The layers may all be of different thickness and viscosity. Also, contacts between layers may have different properties—ranging from freely slipping to bonded. The theoretical basis for the model is the deformation of an interface between two fluids. This is the basic problem in folding theory, and exact solutions for the evolution of an interface were derived by Fletcher (1974, 1977) and Smith (1975). Johnson & Fletcher (submitted) provide an exhaustive treatment of viscous folding.

Basic equations

Viscous folding theory analyzes the deformation within layers of Newtonian (linear-viscous) material in response to stresses and velocities applied at the boundaries. For folding, an essential deformation is layer-parallel shortening. In this theory the two-dimensional Navier–Stokes equations for incompressible, steady, creeping flow are solved under conditions of plane deformation (e.g. Smith 1975, Fletcher 1977, Pfaff 1986, Johnson & Fletcher submitted). Fletcher (1991) has extended the formulation to three dimensions.

A perturbation method which separates components of velocity and stress into mean and perturbed values is used to solve problems in folding. For example, each component of velocity (e.g. v_x) is the sum of the mean velocity, $\bar{v}_x$, and the perturbed velocity, $\tilde{v}_x$:

$$v_x = \bar{v}_x + \tilde{v}_x; \qquad v_z = \bar{v}_z + \tilde{v}_z$$

and each component of stress is the sum of mean and perturbed values;

$$\sigma_{xx} = \bar{\sigma}_{xx} + \tilde{\sigma}_{xx}; \qquad \sigma_{zz} = \bar{\sigma}_{zz} + \tilde{\sigma}_{zz};$$
$$\sigma_{xz} = \bar{\sigma}_{xz} + \tilde{\sigma}_{xz}.$$

The mean flow is the flow that results from layer-parallel compression of flat interfaces, and the per-

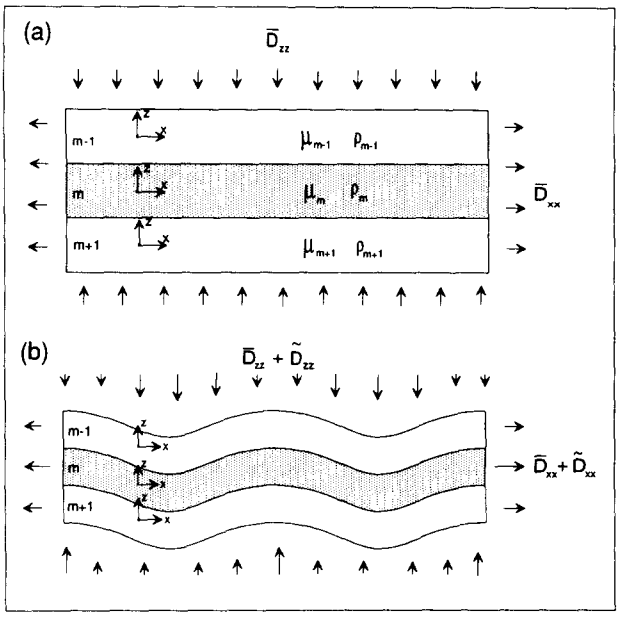

Fig. 2. The evolution of an interface between two fluids undergoing shortening is solved by summing the flow due to shortening where the interface is planar (a) with the flow due to perturbations in the interface (b). Each layer has its own local co-ordinate system.

turbed flow results from shapes of actual deflected interfaces (Fig. 2). Each of the two flows is discussed in more detail below.

Mean flow

The mean flow is the flow resulting from shortening (at a rate of $\bar{D}_{xx}$) parallel to flat interfaces separating viscous fluids (Fig. 2). For incompressible flow $\bar{D}_{zz} = -\bar{D}_{xx}$, and the velocities and stresses in an arbitrary layer m are:

$$(\bar{v}_x)_m = x\bar{D}_{xx} \tag{1a}$$

$$(\bar{v}_z)_m = z\bar{D}_{zz} = -z\bar{D}_{xx} \tag{1b}$$

$$(\bar{\sigma}_{zz})_m = 2\mu_m\bar{D}_{zz} - \bar{p}_m = -2\mu_m\bar{D}_{xx} - \bar{p}_m \tag{1c}$$

$$(\bar{\sigma}_{xx})_m = 2\mu_m\bar{D}_{xx} - \bar{p}_m \tag{1d}$$

$$(\bar{\sigma}_{xz})_m = 2\mu_m\bar{D}_{xz} = 0, \tag{1e}$$

where the deformation rate is

$$\bar{D}_{ij} = \frac{1}{2}\left(\frac{\partial \bar{v}_j}{\partial x_i} + \frac{\partial \bar{v}_i}{\partial x_j}\right).$$

x and z are positions with respect to a local co-ordinate system with an origin at mid-depth in each layer (Fig. 2). For folding to occur, $\bar{D}_{xx}$ is negative (layer-parallel shortening).

The pressure, $\bar{p}_m$, within a layer comes from three sources: an arbitrary confining pressure, a pressure due to density and a pressure from viscosity contrasts between layers. We ignore the effect of gravity, which is satisfactory if density contrasts between layers are negligible, so the pressure due to gravity is essentially hydrostatic. Fletcher (1967) and Nasir & Dabbousi (1978) included the effect of density, but did not include layer-parallel shortening.

The vertical stresses at a horizontal interface must match, so

$$[\bar{\sigma}_{zz}]_{z=-h_m/2} = [\bar{\sigma}_{zz}]_{z=(h_{m+1})/2},$$

where h is the thickness of a layer. Thus, in general, the pressure in layer $(m + 1)$ is:

$$\bar{p}_{(m+1)} = \bar{p}_m + 2(\mu_m - \mu_{(m+1)})\bar{D}_{xx}, \tag{1f}$$

where $\bar{p}_m$ can be set equal to zero for the uppermost layer, or medium $(m = 0)$. The last term is the contribution of the viscosity contrast to the pressure.

Equations (1) provide a complete description of the mean flow.

Perturbed flow

The perturbed flow arises because the interface is not flat. Although an interface is initially perturbed with a single cosinusoidal waveform, the perturbed flow alters the shape of the interface; these deviations from the initial perturbation also contribute to the perturbed flow. For each layer, the basic equations that must be satisfied by the perturbed flow are the two equations for pressure in that fluid:

$$\frac{\partial \tilde{p}}{\partial x} = \mu\left(\frac{\partial^2 \tilde{v}_x}{\partial x^2} + \frac{\partial^2 \tilde{v}_x}{\partial z^2}\right) \tag{2a}$$

$$\frac{\partial \tilde{p}}{\partial z} = \mu\left(\frac{\partial^2 \tilde{v}_z}{\partial x^2} + \frac{\partial^2 \tilde{v}_z}{\partial z^2}\right) \tag{2b}$$

and the biharmonic equation in terms of the stream function, ψ:

$$\frac{\partial^4 \psi}{\partial x^4} + 2\left(\frac{\partial^4 \psi}{\partial x^2 \partial z^2}\right) + \frac{\partial^4 \psi}{\partial z^4} = 0. \tag{2c}$$

$\tilde{v}_x$ is the perturbed velocity in the x-direction, $\tilde{v}_z$ the velocity in the z-direction, and $\tilde{p}$ is pressure;

$$\tilde{p} = -\tfrac{1}{2}(\tilde{\sigma}_{xx} + \tilde{\sigma}_{zz}).$$

The velocity components are related to the stream function through the relations,

$$\tilde{v}_x = -\frac{\partial \psi}{\partial z}; \qquad \tilde{v}_z = \frac{\partial \psi}{\partial x}.$$

A solution to equation (2c) for a cosine-shaped interface between two fluids, is:

$$\psi = (1/l)\{[a + b(lz)]\,e^{lz} + [c + d(lz)]\,e^{-lz}\}\sin(lx).$$

From this solution and the solution of equations (2a) and (2b) for the perturbed pressure, the equations for the perturbed velocity and stress components throughout the fluid are:

$$\tilde{v}_x = -[\{a + b(lz + 1)\}\,e^{lz} - \{c + d(lz - 1)\} \times e^{-lz}]\sin(lx) \tag{3a}$$

$$\tilde{v}_z = [\{a + b(lz)\}\, e^{lz} + \{c + d(lz)\}\, e^{-lz}] \cos(lx) \tag{3b}$$

$$\tilde{\sigma}_{xx} = -2\mu l[\{a + b(lz + 2)\}\, e^{lz} - \{c + d(lz - 2)\} \times e^{-lz}] \cos(lx) + \rho g z - \tilde{p}_o \tag{3c}$$

$$\tilde{\sigma}_{zz} = 2\mu l[\{a + b(lz)\}\, e^{lz} - \{c + d(lz)\}\, e^{-lz}] \times \cos(lx) + \rho g z - \tilde{p}_o \tag{3d}$$

$$\tilde{\sigma}_{xz} = -2\mu l[\{a + b(lz + 1)\}\, e^{lz} + \{c + d(lz - 1)\} \times e^{-lz}] \sin(lx), \tag{3e}$$

where l is the wave number, $l = (2\pi/L)$, and L is the wavelength of the perturbation.

These equations are exact. The central problem in folding theory is evaluation of the arbitrary constants, $\tilde{p}_o$, a, b, c and d for relevant boundary conditions. This is accomplished in two quite different ways in the analytical approach (e.g. Fletcher 1977, Pfaff 1986) and in the numerical approach being followed here. In the analytical approach, one evaluates the constants to a certain order or approximation defined in terms of the maximum slope of a waveform describing the interfaces. In the numerical approach, one sums a series of solutions like those presented in equations (3) and then determines the set of constants that in some sense minimizes the error in matching conditions at the interfaces. Thus the total perturbed flow is the sum of a series of sinusoidal solutions for the flow:

$$(\tilde{v}_x)_m = \sum_{n=1}^{k} -[(a_{mn} + b_{mn}(nlz + 1))\, e^{nlz} - (c_{mn} + d_{mn}(nlz - 1))\, e^{-nlz}] \times \sin(nlx) + O(k + 1) \tag{4a}$$

$$(\tilde{v}_z)_m = \sum_{n=1}^{k} [(a_{mn} + b_{mn}(nlz))\, e^{nlz} + (c_{mn} + d_{mn}(nlz))\, e^{-nlz}] \times \cos(nlx) + O(k + 1) \tag{4b}$$

$$(\tilde{\sigma}_{xx})_m = \sum_{n=1}^{k} -2\mu_m nl[(a_{mn} + b_{mn}(nlz + 2))\, e^{nlz} - (c_{mn} + d_{mn}(nlz - 2))\, e^{-nlz}] \times \cos(nlx) - (\tilde{p}_o)_m + O(k + 1) \tag{4c}$$

$$(\tilde{\sigma}_{zz})_m = \sum_{n=1}^{k} 2\mu_m nl[(a_{mn} + b_{mn}(nlz))\, e^{nlz} - (c_{mn} + d_{mn}(nlz))\, e^{-nlz}] \cos(nlx) - (\tilde{p}_o)_m + O(k + 1) \tag{4d}$$

$$(\tilde{\sigma}_{xz})_m = \sum_{n=1}^{k} -2\mu_m nl[(a_{mn} + b_{mn}(nlz + 1))\, e^{nlz} + (c_{mn} + d_{mn}(nlz - 1))\, e^{-nlz}] \times \sin(nlx) + O(k + 1) \tag{4e}$$

$$(\tilde{p}_o)_m = \text{constant}. \tag{4f}$$

Here k is the number of terms in the series, m is the layer number, and nl is the wave number. $O(k + 1)$ represents all terms truncated from the series.

Equations (4) reduce to equations with two unknown constants for each term in the series for infinite media; such media are used in mathematical models to confine a multilayer. For the upper infinite medium, terms involving a_{mn} and b_{mn} will disappear. For the lower infinite medium terms involving c_{mn} and d_{mn} disappear.

Each equation for a perturbed stress or velocity has $4k$ undetermined constants per layer, and $2k$ undetermined constants for the enclosing infinite media. There are no undetermined constants for the mean flow.

Boundary matching conditions

The flow that results from shortening an interface between two fluids has been described in terms of mean and perturbed components, and the perturbed flow equations involve undetermined constants. In order to solve for the constants, boundary conditions describing relationships between the stress and velocity components must be formulated.

Boundary conditions require that velocities and stresses are matched at an inclined interface, thus we need equations that relate stresses and velocities in the x- and z-directions to directions normal and parallel to the interface (Fig. 3):

$$v_n = -\sin\theta[v_x]_\zeta + \cos\theta[v_z]_\zeta \tag{5a}$$

$$v_s = \cos\theta[v_x]_\zeta + \sin\theta[v_z]_\zeta \tag{5b}$$

$$\sigma_{nn} = [\sigma_{zz}]_\zeta \cos^2\theta + [\sigma_{xx}]_\zeta \sin^2\theta - 2[\sigma_{xz}]_\zeta \cos\theta \sin\theta \tag{6a}$$

$$\sigma_{ns} = [\sigma_{zz} - \sigma_{xx}]_\zeta \cos\theta \sin\theta + [\sigma_{xz}]_\zeta(\cos^2\theta - \sin^2\theta) \tag{6b}$$

where ζ is the z-co-ordinate of a point on an interface, and parameters in brackets, $[\ ]_\zeta$, indicate that the parameter is evaluated at the interface. v_n and σ_{nn} are normal to the interface, v_s and σ_{ns} are parallel to the interface, and θ is the slope angle of the interface.

For multilayers with *bonded* contacts we require that interfaces between layers do not separate or slip. Thus the boundary conditions are:

$$[v_n]_{\zeta_b} = [v_n]_{\zeta_t}; \qquad [v_s]_{\zeta_b} = [v_s]_{\zeta_t}$$

$$[\sigma_{nn}]_{\zeta_b} = [\sigma_{nn}]_{\zeta_t}; \qquad [\sigma_{ns}]_{\zeta_b} = [\sigma_{ns}]_{\zeta_t},$$

where ζ_t is the upper interface of layer $m + 1$, and ζ_b is the lower interface of layer m.

When the contacts between layers are allowed to *slip freely*, the boundary conditions are:

$$[v_n]_{\zeta_b} = [v_n]_{\zeta_t}; \qquad [\sigma_{nn}]_{\zeta_b} = [\sigma_{nn}]_{\zeta_t}$$

$$[\sigma_{ns}]_{\zeta_b} = 0; \qquad [\sigma_{ns}]_{\zeta_t} = 0.$$

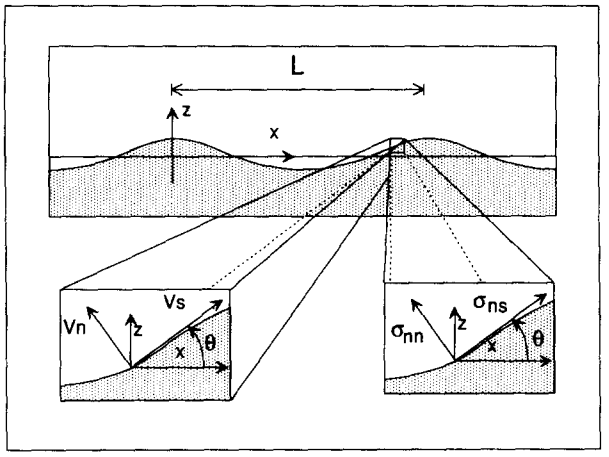

Fig. 3. Boundary conditions in viscous folding theory are formulated in terms of velocities and stresses in directions locally parallel and normal to the interface.

Below we formulate the equations for bonded contacts, since this is the most complete case. Matching velocities at the lower interface of a layer, ζ_b, and the upper interface of the next lowest layer, ζ_t, and noting that the mean velocities cancel:

$$[v_n]_{\zeta_b} - [v_n]_{\zeta_t} = -\sin\theta([\tilde{v}_x]_{\zeta_b} - [\tilde{v}_x]_{\zeta_t}) + \cos\theta([\tilde{v}_z]_{\zeta_b} - [\tilde{v}_z]_{\zeta_t}) = 0 \quad (7)$$

$$[v_s]_{\zeta_b} - [v_s]_{\zeta_t} = \cos\theta([\tilde{v}_x]_{\zeta_b} - [\tilde{v}_x]_{\zeta_t}) + \sin\theta([\tilde{v}_z]_{\zeta_b} - [\tilde{v}_z]_{\zeta_t}) = 0. \quad (8)$$

The normal-stress matching condition is:

$$2\bar{D}_{xx}(\mu_{m+1} - \mu_m)\sin^2\theta = ([\tilde{\sigma}_{zz}]_{\zeta_b} - [\tilde{\sigma}_{zz}]_{\zeta_t})\cos^2\theta + ([\tilde{\sigma}_{xx}]_{\zeta_b} - [\tilde{\sigma}_{xx}]_{\zeta_t}) \times \sin^2\theta - 2([\tilde{\sigma}_{xz}]_{\zeta_b} - [\tilde{\sigma}_{xz}]_{\zeta_t})\cos\theta\sin\theta, \quad (9)$$

and for bonded contacts the shear stress matching condition is:

$$-4\bar{D}_{xx}(\mu_{m+1} - \mu_m)\cos\theta\sin\theta = ([\tilde{\sigma}_{zz} - \tilde{\sigma}_{xx}]_{\zeta_b} - [\tilde{\sigma}_{zz} - \tilde{\sigma}_{xx}]_{\zeta_t})\cos\theta\sin\theta + ([\tilde{\sigma}_{xz}]_{\zeta_b} - [\tilde{\sigma}_{xz}]_{\zeta_t})(\cos^2\theta - \sin^2\theta). \quad (10)$$

A variation on the free-slip or bonded contact boundary condition is a contact that is allowed to slip, but resists slip according to some relation. For a bonded contact, the velocity difference across the interface was specified to be zero. However we can specify the velocity difference in terms of a film viscosity, μ_f, and a film thickness, h_f, and relate the velocity difference to the shear stress at the interface (Fig. 1). Large viscosities will allow little or no slip, while low viscosities will permit slip at the interface. Specifying the ratio h_f/μ_f allows any behavior from free-slip to fully bonded to be modeled. Johnson & Pfaff (1989) and Pfaff & Johnson (1989) used a power-law rheology to relate the change in velocity across a contact. This allowed areas of high contact shear stress to slip (e.g. inflection points on fold limbs), while other areas were effectively still bonded (e.g. fold hinge zones). In our analysis of high-amplitude folding, however, we have restricted ourselves to viscous drag.

For viscous resistance to slip, the shear velocity matching condition becomes:

$$[v_s]_{\zeta_b} - [v_s]_{\zeta_t} = \left(\frac{h_f}{\mu_f}\right)\sigma_{ns},$$

where h_f is the thickness of a viscous film at the contact, and μ_f is the viscosity of the film. For viscous slip the following equation would replace equation (8):

$$-4\bar{D}_{xx}\mu_m(h_f/\mu_f)\cos\theta\sin\theta = [v_s]_{\zeta_b} - [v_s]_{\zeta_t} - \{([\tilde{\sigma}_{zz} - \tilde{\sigma}_{xx}]_{\zeta_b}\cos\theta\sin\theta + [\tilde{\sigma}_{xz}]_{\zeta_b}(\cos^2\theta - \sin^2\theta)\}(h_f/\mu_f). \quad (11)$$

Below we expand the normal-velocity matching conditions, and group the terms according to the constants. Substituting the velocity equations (3a) and (3b) into equation (7) and grouping terms,

$$\begin{aligned}
0 = {} & a_{(m-1)n}\{\sin\theta[e^{lz}\sin(lx)]_{\zeta_b} + \cos\theta[e^{lz}\cos(lx)]_{\zeta_b}\} \\
& + a_{mn}\{\sin\theta[e^{lz}\sin(lx)]_{\zeta_t} - \cos\theta[e^{lz}\cos(lx)]_{\zeta_t}\} \\
& + b_{(m-1)n}\{\sin\theta[e^{lz}\sin(lx)(lz+1)]_{\zeta_b} \\
& \quad + \cos\theta[e^{lz}\cos(lx)lz]_{\zeta_b}\} \\
& + b_{mn}\{\sin\theta[-e^{lz}\sin(lx)(lz+1)]_{\zeta_t} \\
& \quad - \cos\theta[e^{lz}\cos(lx)lz]_{\zeta_t}\} \\
& + c_{(m-1)n}\{\sin\theta[-e^{-lz}\sin(lx)]_{\zeta_b} \\
& \quad + \cos\theta[e^{-lz}\cos(lx)]_{\zeta_b}\} \\
& + c_{mn}\{\sin\theta[e^{-lz}\sin(lx)]_{\zeta_t} \\
& \quad - \cos\theta[e^{-lz}\cos(lx)]_{\zeta_t}\} \\
& + d_{(m-1)n}\{\sin\theta[-e^{-lz}\sin(lx)(lz-1)]_{\zeta_b} \\
& \quad + \cos\theta[e^{-lz}\cos(lx)lz]_{\zeta_b}\} \\
& + d_{mn}\{\sin\theta[e^{-lz}\sin(lx)(lz-1)]_{\zeta_t} \\
& \quad - \cos\theta[e^{-lz}(lx)lz]_{\zeta_t}\}. \quad (12)
\end{aligned}$$

Similar equations can be written for the other three matching conditions. The remainder of the theoretical section deals with determining the constants once their coefficients have been calculated.

LEAST-SQUARES DETERMINATION OF CONSTANTS TO FOLDING EQUATIONS

The objective is to determine values for the constants which can be used to calculate stresses and velocities in a multilayer. Previously this has been done algebraically for a limited number of terms in equation (4) (e.g. Fletcher 1977, Pfaff 1986). Here we do it numerically for an arbitrary number of terms. Before developing the solution method, we first show that we have a sufficient number of equations to solve for the unknown constants.

In a multilayer composed of m layers, ($m - 2$ finite layers, and two infinite confining media) there are

$4(m-1)$ constants (four per layer, two per media) and $(m-1)$ interfaces. Using the four matching conditions (v_n, v_s, σ_{nn}, σ_{ns}) at one point on each interface gives a total of $4(m-1)$ equations, which is sufficient to solve for all the constants in the multilayer.

The constants determined using only one point on each interface will exactly satisfy velocity and stress boundary conditions at these points, however, there will not be very good agreement in the matching conditions away from these points (Fletcher 1967, Nasir & Dabbousi 1978). The equations will better represent the velocity and stress distributions over the entire interface if the constants are over-determined, and chosen so that they best fit the matching conditions in a least-squares sense (e.g. Dahlquist & Björck 1974, Stoer & Bulirsch 1980). The velocity and stress distribution equations may not be anywhere exactly satisfied, however, the velocity and stress at an arbitrary point can be calculated with less error than if only the minimum number of points were used.

The reason we use least squares is because of the nonlinearity of the problem. The non-linearity enters only through the boundary conditions. We illustrate the nature of the non-linearity by expanding a single term from equation (12). We have chosen the coefficient for b_{mn}:

$$\sin\theta[-e^{lz}\sin(lx)(lz+1)]_{\zeta_t} - \cos\theta[e^{lz}\cos(lx)lz]_{\zeta_t}.$$

At the interface, $z=\zeta$, the coefficient is written as:

$$\sin\theta\{-e^{l\zeta}\sin(lx)(l\zeta+1)\} - \cos\theta\{e^{l\zeta}\cos(lx)l\zeta\},$$

where

$$\sin\theta = \frac{\dfrac{\partial\zeta}{\partial x}}{\sqrt{1+\left(\dfrac{\partial\zeta}{\partial x}\right)^2}}; \qquad \cos\theta = \frac{1}{\sqrt{1+\left(\dfrac{\partial\zeta}{\partial x}\right)^2}}.$$

Thus the coefficient becomes,

$$\frac{\dfrac{\partial\zeta}{\partial x}}{\sqrt{1+\left(\dfrac{\partial\zeta}{\partial x}\right)^2}}\{-e^{l\zeta}\sin(lx)(l\zeta+1)\}$$

$$-\frac{1}{\sqrt{1+\left(\dfrac{\partial\zeta}{\partial x}\right)^2}}\{e^{l\zeta}\cos(lx)l\zeta\}.$$

Similar expressions can be written for each of the terms in equation (12). The essential non-linearity of the problem in the variable x is apparent if we represent the interface with a finite Fourier series,

$$\zeta_t = h_m/2 + A_1\cos(lx) + A_2\cos(2lx) + A_3\cos(3lx) + \ldots + A_n\cos(nlx)$$

in which A_n is the amplitude of the n-th waveform.

In analyzing the growth of a fold, the height of the top of the layer, ζ_f is initially $h_m/2 + A_1\cos(lx)$, in which h_m is the thickness of the layer, and A_1 is the amplitude of a cosine waveform, and is a component of an eigenvector of amplitudes (Johnson & Pfaff 1989). The cosine waveform is the initial perturbation of the interfaces. During growth of the fold, however, each interface is represented by a piecewise cubic spline. A piecewise cubic spline is a set of coefficients for a cubic equation, with a set of coefficients for each interval between points representing the interface. The coefficients are chosen so that first- and second-derivatives are continuous along the interface (Stoer & Bulirsch 1979). By representing the interface with a spline, the function will pass through all points used to represent the interface, something not guaranteed by a finite Fourier series.

We now derive the least-squares solution, and illustrate that it provides the best numerical estimate for the constants. At each point on the interface the normal and shear stresses and velocities above and below the interface are matched. This gives the four equations for each point required to determine the constants. Thus, for a single matching condition at any point on an interface, we have an equation of the form:

$$A_{i1}C_1 + A_{i2}C_2 + A_{i3}C_3 + A_{i4}C_4 + \ldots + A_{iK}C_K = D_i,$$

where A_{iK} is a coefficient to a constant, C_j is a constant and D_i is the driving term. K is the number of undetermined constants in the multilayer. Matching at n points on m interfaces for k terms in the perturbed flow series gives the following set of equations:

$$\begin{aligned}
A_{11}C_1 + A_{12}C_2 + A_{13}C_3 + A_{14}C_4 + \ldots + A_{1K}C_K &= D_1\\
A_{21}C_1 + A_{22}C_2 + A_{23}C_3 + A_{24}C_4 + \ldots + A_{2K}C_K &= D_2\\
A_{31}C_1 + A_{32}C_2 + A_{33}C_3 + A_{34}C_4 + \ldots + A_{3K}C_K &= D_3\\
&\vdots\\
A_{N1}C_1 + A_{N2}C_2 + A_{N3}C_3 + A_{N4}C_4 + \ldots + A_{NK}C_K &= D_N,
\end{aligned}$$

where $N = 4\times m\times n$ and $K = 4\times m\times k$.

This set of equations can be written using subscript notation:

$$A_{ij}C_j = D_i,$$

where i ranges from 1 to N, and j ranges from 1 to K.

We define a residual, R, which is the difference between the actual value D, and the value computed using some estimate of the constants, C_j. For a single point and matching condition, the equation becomes

$$A_{i1}C_1 + A_{i2}C_2 + A_{i3}C_3 + A_{i4}C_4 + \ldots + A_{iK}C_K - D_i = R_i.$$

R_i, D_i and C_j must all have the same dimensions. This implies that A_{ij} is dimensionless. For the entire multilayer the equations become, in subscript notation:

$$A_{ij}C_j - D_i = R_i. \quad (13)$$

An estimate of the total error is the sum of the R values. However, individual R values may have different signs, so an unbiased measure of the error, M, is the sum of the squares of the residuals, R,

$$M = \sum_{i=1}^{N} R_i^2 = R_1^2 + R_2^2 + R_3^2 + \ldots R_N^2 = R_p R_p.$$

The total error, M, is minimized when $\partial M/\partial C_j$ is zero. For the differentiation, the actual values of constants, C_j, need not be known. Taking the derivative of M with respect to the first constant, C_1, gives

$$\frac{\partial M}{\partial C_1} = 0 = \frac{\partial R_1^2}{\partial C_1} + \frac{\partial R_2^2}{\partial C_1} + \frac{\partial R_3^2}{\partial C_1} + \ldots + \frac{\partial R_N^2}{\partial C_1}$$

$$\frac{\partial R_1^2}{\partial C_1} = \frac{\partial}{\partial C_1}(A_{11}C_1 + A_{12}C_2 + A_{13}C_3 + \ldots + A_{1(4k)}C_{4k} - D_1)^2$$

$$= 2A_{11}(A_{1j}C_j - D_1).$$

Similar expressions can be derived for the other terms:

$$\frac{\partial R_2^2}{\partial C_1} = 2A_{21}(A_{2j}C_j - D_2),$$

$$\frac{\partial R_3^2}{\partial C_1} = 2A_{31}(C_j - D_3), \text{ etc.}$$

Summing terms,

$$\frac{\partial M}{\partial C_1} = 2A_{i1}(A_{ij}C_j - D_i).$$

In general,

$$\frac{\partial M}{\partial C_p} = 2A_{ip}(A_{ij}C_j - D_i).$$

The error is minimized when $\partial M/\partial C_p$ is zero:

$$2A_{ip}(A_{ij}C_j - D_i) = 0.$$

This can be written in the following form:

$$A_{ip}A_{ij}C_j - A_{ip}D_i = 0.$$

The subscripts p and j range from 1 to K, the number of constants, and the subscript i ranges from 1 to N, the number of matching equations. This equation gives the following square matrix:

$$\begin{vmatrix} A_{i1}A_{i1} & A_{i1}A_{i2} \ldots A_{i1}A_{iK} \\ A_{i2}A_{i1} & A_{i2}A_{i2} \ldots A_{i2}A_{iK} \\ A_{i3}A_{i1} & A_{i3}A_{i2} \ldots A_{i3}A_{iK} \\ & \vdots \\ A_{iK}A_{i1} & A_{iK}A_{i2} \ldots A_{iK}A_{iK} \end{vmatrix} \begin{vmatrix} C_1 \\ C_2 \\ C_3 \\ \vdots \\ C_K \end{vmatrix} = \begin{vmatrix} A_{i1}D_i \\ A_{i2}D_i \\ A_{i3}D_i \\ \vdots \\ A_{iK}D_i \end{vmatrix}.$$

Comparing the cell (2,1) (row 2, column 1) with cell (1,2), and cell ($4k$,1) with cell (1,$4k$), it can be seen that they are identical. This indicates that the matrix is diagonally symmetric. For any cell in the matrix, the only repeated subscript is i, the row counter. Thus, for any cell in the matrix, we sum on i. This indicates that the matrix can be generated by manipulating only one row of the A matrix at a time, rather than multiplying two complete A matrices.

The constants, C_j, which minimize the residuals (equation 13) can then be solved for by inverting the coefficient matrix. Computationally, it is unnecessary to completely invert the matrix, and we use a LU-decomposition with back substitution to solve for the constants (e.g. Dahlquist & Björck 1974, Stoer & Bulirsch 1980).

Procedure

The least-squares method requires that the equations be dimensionless, and we have used the uppermost layer as the characteristic layer: all thicknesses, lengths, viscosities and densities are normalized with the properties of this layer. Once a multilayer model has been constructed we use the method of Johnson & Pfaff (1989, pp. 152–154) to calculate the dominant and preferred wavelengths, as well as the initial wavelength that becomes the preferred wavelength at the end of folding. The folds are seeded by perturbing the interfaces with a single cosine waveform of 1° maximum slope. The relationship between dominant and preferred wavelength is simple, as shown by Johnson & Pfaff (1989, p. 152).

The constants in equation (4) are determined for the initial conditions, and used to calculate velocities of material points on the interfaces. These velocities are integrated to give the new positions for the material points after some increment of deformation, and the constants for the new interface shape are calculated. At each increment material points on the interfaces are arranged so that they are uniformly distributed along the interface. The interface is represented by a cubic spline (Stoer & Bulirsch 1980). Accuracy in the integration step is essential, and we use a Runge–Kutta integration procedure that is accurate to fourth-order in the step size (Stoer & Bulirsch 1980). (This differs from the first-order, Euler method used in finite-element studies. The Euler integration procedure simulates folds of lower amplitude than the Runge–Kutta method, which is to be expected when integrating an exponential function.) The program continues tracing the interface positions until either a specified amount of shortening has occurred, or a maximum error limit has been exceeded.

Suitability of the solution

The solutions presented in following pages have all passed several suitability tests. Each of the tests is a necessary but insufficient condition for correctness. During a simulation the program monitors the squared residuals (equation 13), the correlation coefficient (r^2), the v_n mismatch across an interface, and the conservation of volume. The most critical of these conditions is the v_n mismatch, for, without good velocities, the integration, no matter how precise, would be inaccurate.

We have set a criterion that only solutions with v_n mismatch of less than 1% of the maximum v_n are acceptable. Solutions with a maximum v_n mismatch greater than 1% are not known to be incorrect. Indeed, symmetry in some cases is maintained until much larger mismatches occur. However, there is no reason to trust such solutions. A mismatch of about 1% occurs when the constants of the last term in the perturbed flow series begin to become significant, suggesting that the next term in the series would also be significant. At this stage, the simulation could be re-run with more terms in the series.

In addition to the tests described above, symmetry was also used to check solutions for single layers and symmetric multilayers. The simulations are set up so that no symmetry is imposed. A complete wavelength is used, and the velocities on an interface are calculated using the constants from the overlying material. Thus, in a single layer the velocities of the upper interface are calculated using media constants, and the velocities of the lower interface using layer constants. With the model set up in this manner interface shapes could be used as an internal check.

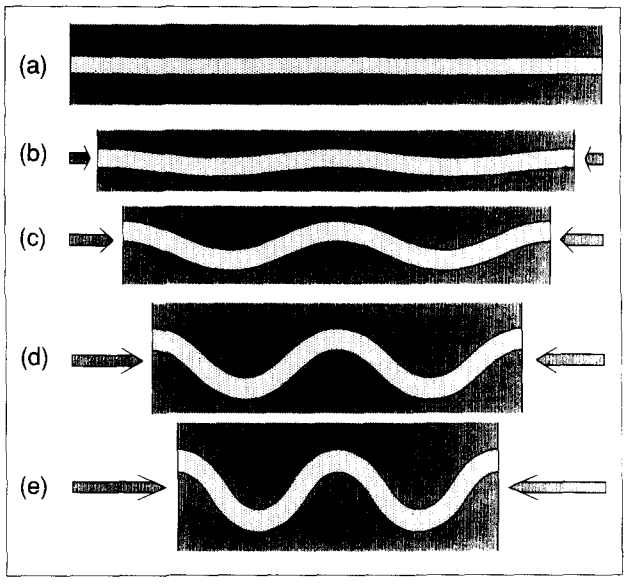

Fig. 4. Five stages in the development of a single-layer fold composed of a material 50 times stiffer than the medium. There is an equal amount of shortening between each step. Boundary conditions were matched at 161 points on each interface. The series solution for the perturbed flow used 10 terms.

RESULTS

Below we present results of analyses using least-squares to determine constants that minimize mismatch of stresses and velocities at interfaces, and using the algorithm outlined above. All the analyses presented used free-slip at contacts. The analyses were all stopped when the maximum v_n mismatch reached about 1% of the maximum normal velocity. Results at every stage are saved and can be animated. Unfortunately, here we can only provide snapshots of the evolution of the fold.

We first present results for a single layer embedded in identical media. This is the most common analysis of folding, and we include these analyses for comparison with previous studies. We also present results for symmetric multilayers, again to demonstrate that the solution produces no unexpected results. These multilayers also help temper one's intuition about how more complex multilayers can be modeled. The section ends with a simulation of folds in two more complicated multilayers.

Single layer

Perhaps the most thoroughly studied fold is the single-layer fold. The majority of theoretical studies have focused on a competent layer in less competent media. We first re-examine this problem.

The solution derived here was verified at low amplitude (maximum limb slopes less than 10°) by checking the numerical values of constants with those computed with the analytical solutions of Fletcher (1977) and Johnson & Fletcher (submitted). Cases involving both bonded and free-slip contacts were checked, and the constants differed by less than 10^{-4}% at low amplitudes. Also, the form of a fold with a maximum limb slope of 24° was checked against the form calculated using a third-order analysis (Johnson & Fletcher submitted). The fold forms were indistinguishable.

Figure 4 shows the evolution of a single layer between two infinite media. The viscosity of the layer is 50 times that of the media, and the contacts could slip freely. Figure 4(a) shows the initial perturbation. It has a maximum slope of 1° and is perturbed with a wavelength 16 times the layer's thickness. Ten terms were used in the series approximation (equation 4). The boundary conditions were matched over one wavelength at 161 points on each interface. Early in the folding history the layer thickens noticeably, but the fold does not grow much in amplitude. As folding continues, the amplitude of the fold grows rapidly. The fold has maximum slopes of about 40° and has a concentric-like form at the stage shown in Fig. 4(d). The slope has increased to nearly 60° and the hinges show subtle, but noticeable, thickening while there is thinning on the limbs at the stage shown in Fig. 4(e). Although the fold is concentric-like, it is beginning to show some of the characteristics of similar folds.

Figure 5 shows a series of single-layer folds, all with the same initial geometry, and all shortened the same amount. The viscosity contrast between the layer and media increases from 10 in Fig. 5(a) to 100 in Fig. 5(f). With increasing viscosity contrast, the amplitude of the fold increases. At low viscosity contrast, the layer thickens much more than at high viscosity contrasts. It should be noted that for the analyses shown in Fig. 5, the preferred wavelength was not used to seed the solution, since the objective was to show the effect of variation of viscosity contrast on the same initial conditions. Ten terms in the approximation to the perturbed flow were used, and the boundary conditions were matched at 161 points on each interface.

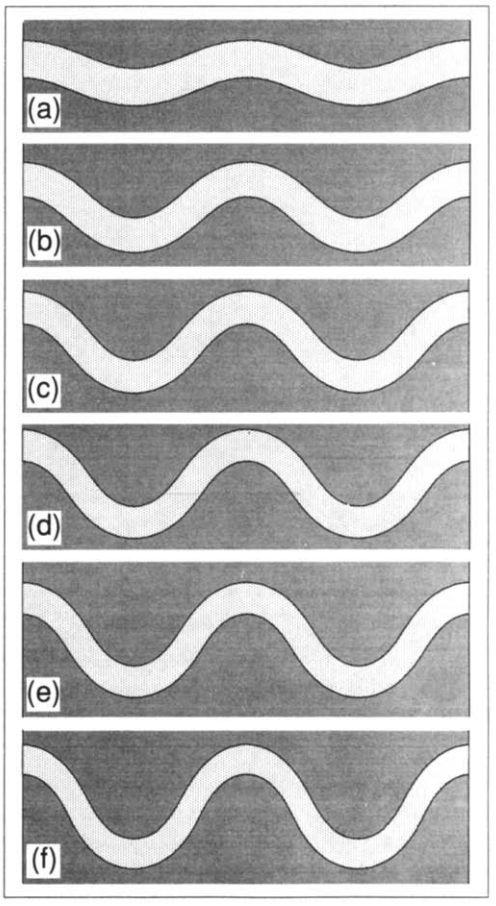

Fig. 5. Variation in fold form for a single layer in identical soft media with changing viscosity contrast. The form for the lowest viscosity ratio (10; the layer is 10 times stiffer than the medium), is shown in (a), and forms for the highest viscosity ratio (100) is shown in (f). The viscosity ratios for the various folds are (a) 10, (b) 20, (c) 30, (d) 40, (e) 50 and (f) 100. All the folds have undergone 40% shortening.

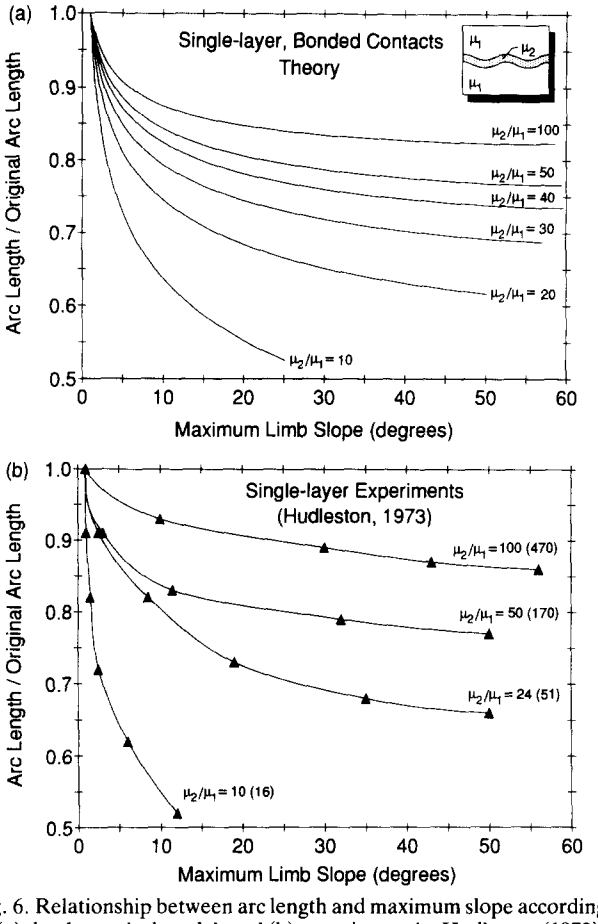

Fig. 6. Relationship between arc length and maximum slope according to (a) the theoretical model, and (b) experiments by Hudleston (1973). The theoretical and experimental results are broadly correlated. The results show that the arc length decreases rapidly until maximum limb slopes are 10–15°. Between 10° and 20° the change in arc length becomes considerably less. When maximum limb slopes are more than 20–25° there is little change in arc length. Hudleston's experiments may have been with non-linear materials. The numbers next to the curves are viscosity ratios based on back-calculation from linear-viscous folding theory. The numbers in parentheses are viscosity ratios measured with a viscometer. Thus, none of the viscosity ratios reported in (b) may be equivalent to those in (a). In the theoretical model, the layers were represented by 161 points, and 10 terms were used in the approximation series. The wavelength was selected so that the wavelength at the end of shortening would be the preferred wavelength. The initial maximum slope angle of the perturbation was 1°.

Hudleston (1973) (see also Hudleston & Stephansson 1973) performed a series of experiments on single-layer folds using viscous material. In these experiments Hudleston noted that there was little change in the arc length of the folds once limb dips of 10–20° had been reached. This was independent of viscosity contrast. Figure 6 shows normalized fold arc-length as a function of maximum limb dip for the solution presented here (Fig. 6a) and for the experiments of Hudleston (Fig. 6b). Results from our solution (Fig. 6a) show a rapid decrease in arc length for slopes less than 10° for all viscosity contrasts. From 10° to 20° the rate of interface shortening decreases. There is very little change in arc length once the slopes are greater than about 25°. The angle above which the arc length does not change becomes smaller as the viscosity contrast increases.

The data shown in Fig. 6(b) are from Hudleston's experiments (Hudleston & Stephansson 1973, fig. 3). Hudleston used solutions of ethyl cellulose in benzyl alcohol for his experiments. At concentrations of 15% or less ethyl cellulose the solutions are almost true Newtonian fluids, however at higher concentrations they may be weakly nonlinear (Hudleston 1973, p. 193). In the experimental results shown in Fig. 6(b) the concentrations were of the order of 28–40% ethyl cellulose (Hudleston 1973, table 1), so the layers may have been behaving as non-linear fluids. This could explain why the wavelength-to-thickness ratios observed by Hudleston were smaller than expected from a linear-viscous folding theory (Smith 1979, p. 284).

Unfortunately, there is considerable confusion concerning the viscosity ratios reported by Hudleston (1973). The viscosity ratios shown for the curves in Fig. 6(b) were *calculated* by Hudleston, using an approximate theoretical analysis of fold wavelength and amplification. The viscosity ratios he measured, with a viscometer, are shown in parentheses. These values are alarmingly different. Thus, the viscosity ratios reported in Figs. 6(a) & (b) cannot be easily compared. Nevertheless, the curves for the experiments of Hudleston are *qualitatively* similar to the curves derived with the theoretical analysis presented here.

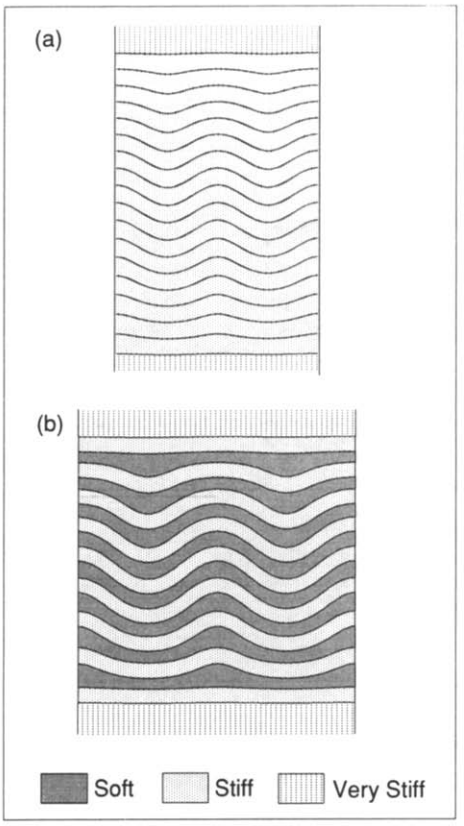

Fig. 7. Constrained fold forms in multilayers confined by stiff media. Each multilayer consists of 17 layers. In (a) the layers have the same viscosity, and the media are 100 times stiffer than the layers, (b) shows the folding where the multilayer consists of alternating stiff and soft layers. The stiff layers have a viscosity 10 times that of the soft layers, and the media have a viscosity 100 times that of the stiff layers (1000 times the soft layers).

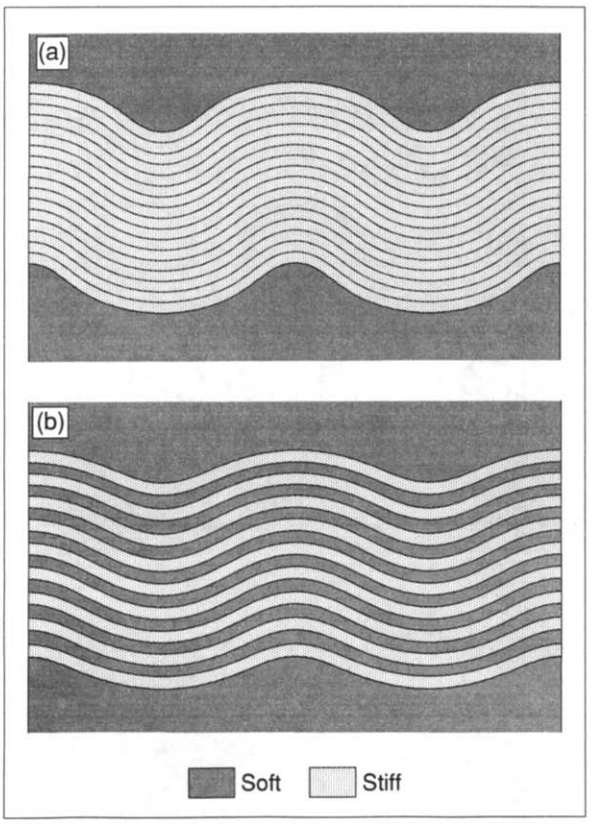

Fig. 8. Concentric-like folds in multilayers confined by soft media. Each multilayer consists of 17 layers. In (a) the layers have the same viscosity, and are 10 times stiffer than the media. In (b) the multilayer consists of alternating stiff and soft layers in which the stiff layers are 10 times as stiff as the soft layers.

Symmetric, repetitive multilayers

Freely-slipping contacts are used so that multilayer folding can be analyzed. The choice of contact property has little influence on the final fold form. In multilayers, amplification factors for bonded contacts are much lower than for freely-slipping contacts (Johnson & Pfaff 1989). For a multilayer with bonded contacts there has to be a large amount of shortening to produce folds. For example, consider a multilayer composed of identical layers (e.g. Huasna simulation, below), if bonded contacts were used the entire multilayer would behave as a single thick layer. Field observations of striation along bedding planes show that there is slippage along layer contacts during folding (e.g. Pfaff 1986).

The simplest multilayers are symmetric, and composed of layers of the same viscosity, or alternating beds of two different viscosities (Figs. 7 and 8). Similar multilayers have been analyzed using a third-order solution (Johnson & Pfaff 1989). We present results for four simple multilayers. The first (Fig. 7a) consists of 17 layers of the same viscosity confined by infinite media that are 10 times stiffer than the layers. The second multilayer (Fig. 7b) is also confined by stiff media, however the stiff layers are interbedded with soft layers of 1/10 the viscosity of stiff layers. In both Figs. 7 and 8 stresses and velocities were matched at 161 points on each interface, and 10 terms in equation (4) were used.

For stiff media (Fig. 7), the highest amplitude folds are in the middle of the multilayer, and the amplitudes die out towards the confining media. At low amplitude the form is similar to the 'internal instability' of Biot (1964), but at high amplitudes shown in Fig. 7 the form is the *constrained fold* of Johnson & Pfaff (1989). Synclines and anticlines at mid-depth in the multilayer are equal in size. Up section from mid-depth, the anticlines become broader and flatter while the synclines become narrower and pinched. In Fig. 7(b) the stiff layers are interbedded with softer layers. The synclines do not appear as pinched as in Fig. 7(a), and the soft interbeds accommodate most of the thickening and thinning.

Where the confining media are soft (Fig. 8), and the multilayer is composed of similar beds (Fig. 8a), the entire multilayer folds with no noticeable thickening and thinning of individual layers. Synclines on the upper surface are narrow, but become broader down section. The fold form is concentric-like. It is quite interesting that the cores of the anticlines do not tightly pinch to become chevron folds.

The high-amplitude analysis is consistent with the third-order analysis of Johnson & Pfaff (1989), in that chevron-like folds are absent in normal folding of linear-viscous material (the only result that produced chevron forms, is for an unusually short wavelength, many times

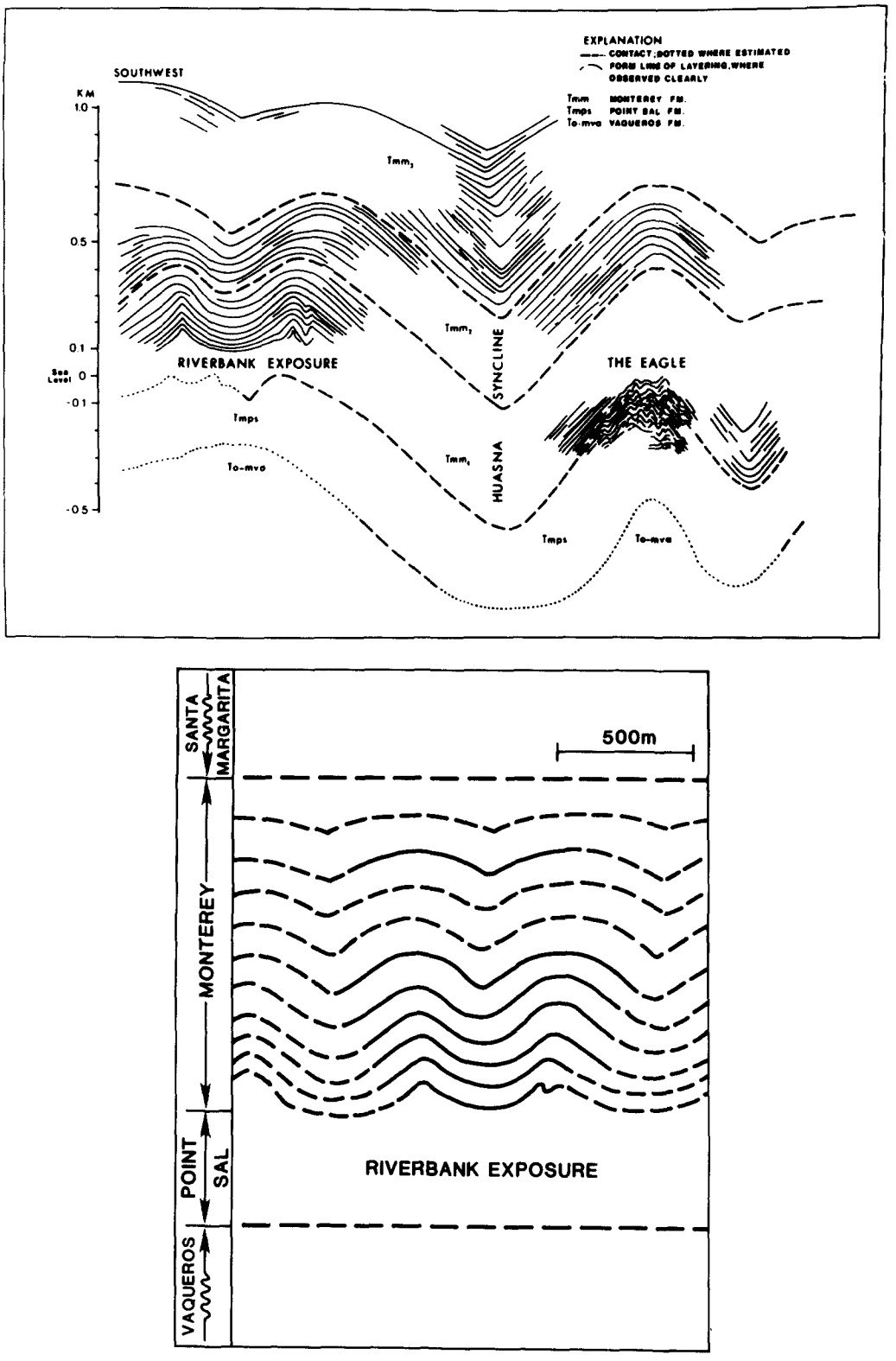

Fig. 9. Folds associated with the Huasna syncline in California. (a) Down-plunge view of the Huasna syncline. (b) Idealized view of folds in the riverbank exposure (after Johnson & Pfaff 1989). The essential elements of fold forms in the riverbank exposure are that amplitudes become lower, synclines become narrower, and anticlines become broader up-section.

shorter than the dominant or preferred wavelength for a multilayer, Johnson & Pfaff 1989, fig. 4). Johnson (1977) concluded that the chevron form is a result of some kind of yielding in hinges. The results presented show that, in a material that cannot yield, the chevron form is missing. They do not show, though, that yielding is a necessary condition of chevron folding.

Figure 8(b) shows folds in a multilayer of interbedded stiff and soft layers. The soft layers have the same viscosity as the confining media, which is 1/10 the viscosity of the stiff layers. The stage shown in Fig. 8(b) has undergone about 22% shortening. Soft layers, in the core of the anticline in the center of the picture show thickening at the hinges low in the multilayer, but thinning near the upper medium. The anticlines also become broader up-section. The same trend, but in

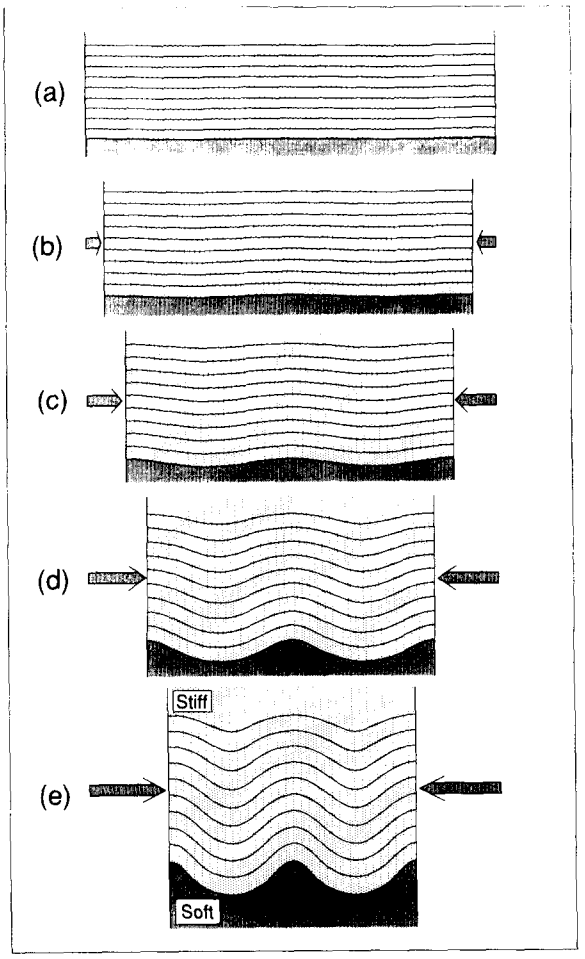

Fig. 10. Simulation of the idealized folds in the riverbank exposure based on linear-viscous model. The structural-lithic units in the riverbank exposure were modeled with nine layers of identical material confined above by a stiff medium, and below by a soft medium. The gross forms of the folds in the riverbank exposure—folds that die out up-section, and narrow anticlines becoming broader up-section—are reproduced by the model. Notably lacking in the linear-viscous folds are the sharpened, chevron-like forms that are so obvious in the field. Initial conditions of the model are shown in (a), and the form after 40% shortening is shown in (e).

reverse, exists in the synclines. The forms are, again, concentric-like and chevron folds are absent.

Huasna syncline

The 'riverbank exposure' part of the Huasna syncline in the southern California Coast Range has been described in detail by Johnson & Page (1976), and its essential characteristics are presented by Johnson & Pfaff (1989). The Huasna syncline is shown in down-plunge view, and the forms visible in the 'riverbank exposure' are idealized in Fig. 9. Folds within the upper Monterey Formation consist of broad anticlines, with narrow, sharp synclines. Down-section, below the Monterey–Santa Margarita contact, the synclines and anticlines become higher in amplitude, and the synclines become broader while the anticlines become narrower.

The Monterey Formation is a series of interbedded shales and porcelanite beds, and is composed of structural–lithic units that are 30–40 m thick, and separated by thin shear zones. The overlying Santa Margarita Formation is a relatively massive sandstone, while the underlying Point Sal Formation is soft shale and dolomite (Johnson & Page 1976, Chen & Oertel 1989).

The field evidence suggests that the Monterey can be modelled as nine layers of equal thickness and viscosity, and the contacts between the layers be allowed to slip freely. The overlying Santa Margarita is modeled as a confining medium, of the same viscosity as the Monterey. The underlying Point Sal is taken to be a soft confining medium with a viscosity of 1/100 the viscosity of the Monterey layers.

The results of an analysis using 10 terms in equation (4) is shown in Fig. 10. The folds in the multilayer have some of the essential elements of the folds in the 'riverbank exposure'. The model shows the amplitude of the folds increasing gradually downward. In the upper layer the synclines are sharper than the anticlines and they become broader down-section. The anticlines become sharper down-section.

Although the same variations can be seen in the forms in the high-amplitude analysis and the down-plunge view, the actual forms of the folds differ. The folds in the Huasna syncline have straighter limbs and sharper hinges. The sharpened, chevron-like forms in the field situation are missing in the theoretical results. Our experience with several theoretical analyses based on linear-viscous theory suggests that we cannot expect the theory to produce the sharpened forms. We suggest that some type of non-linear model, such as a power-law model, would be required to simulate yielding and thereby produce sharp hinges, which so characterize the actual folds.

The Berry–Buffalo syncline

Folding in the Appalachians occurs at several scales (e.g. Nickelsen 1963). Folds with wavelengths of 11–18 km involve rocks from the Cambrian to the Pennsylvanian, while intermediate-scale folds (wavelength of about 3 km) are best developed at the levels of the Silurian Tuscarora and Ordovician Juniata–Bald Eagle Formations (Table 1). The large-wavelength folds appear to be controlled by the massive sandstones of the Devonian Catskill Formation. Folds with intermediate wavelengths occur in the Lower Paleozoic sandstones, apparently because these sandstones are stratigraphically bounded by thick units of less competent rocks, and have a degree of mechanical independence from the Upper Paleozoic units.

In an investigation of Appalachian fold forms, Aytuna (1984) constructed a down-plunge section of the Berry–Buffalo syncline in central Pennsylvania (Fig. 11). The syncline is open, and has straight limbs and narrow hinges in its upper parts. Further down section the hinges become more rounded, and are fairly flat near the base of the section. A Fourier analysis for the interfaces indicates that the shorter waveforms were present lower in the section, and much stronger there than higher in the section.

Based on the forms of the folds in the Berry–Buffalo

Table 1. Average thickness and normalized viscosity ratio of the structural units of the central Appalachians (from Aytuna 1984)

			Average thickness (km)	Normalized viscosity
PENNSYLVANIAN		Llewellyn Formation	1	1
		Pottsville Formation	0.45	100
MISSISSIPPIAN		Mauch-Chunk Formation	0.7	5
		Pocono Formation	0.6	5
DEVONIAN	Catskill Formation	Duncanon Member Clark's Ferry Member	1.5	100
		Sherman Creek Member	0.5	25
		Irish Valley Member	1	100
		Trimmers Rock Formation	0.7	100
	Mahantango Formation or Hamilton Group	Harrell Member Sherman Ridge Member	0.5	30
		Montebello Member		
		Marcellus Formation Onandago Formation Oriskany Formation Helderberg Formation Keyser Formation	0.375	20
SILURIAN		Tolonoway Formation		
		Wills Creek Formation	0.4	1
		Bloomsburg Formation		
		Mifflintown Formation	0.365	1
		Rose Hill Formation		
		Tuscarora Formation	0.2	100
ORDOVICIAN		Juniata Formation	0.25	100
		Bald Eagle Formation		
		Martinsburg Formation (Reedsville Formation)	1	1
CAMBRO-ORDOVICIAN			3	5

syncline, and knowing how ideal multilayers behave (Figs. 8 and 7), we would suppose that the Berry–Buffalo syncline formed in a multilayer confined below by a stiff material and above by a soft material, or perhaps was unconfined above. Thus, in our model of folding in the central Appalachians we use the thickness and viscosity ratios given in Table 1, with a stiff lower medium and a very soft upper medium.

Analysis of eigenvectors and eigenvalues of the folding, according to the central Appalachian stratigraphy shown in Table 1, shows there are two wavelengths that have large amplification factors (Aytuna 1984). The wavelength of one perturbation that amplifies rapidly is about 3.3 km, and the wavelength of the other is about 17 km. For all layers the highest amplification factor was for perturbations with a 17 km wavelength. The 3.3 km wavelength was important only in the lower Paleozoic strata (Tuscarora and Bald Eagle Formations).

Using the theoretical analysis presented here, where the interfaces were seeded with only the 17 km wavelength the folds with shorter wavelengths produced in the Lower Paleozoic were barely noticeable.

Figure 12 shows results of an analysis where the perturbations in the interfaces were seeded with both the 17 and 3.3 km wavelengths. Folds became broader down-section, and have very flat bottoms, in this respect they are similar to the folds shown in the down-plunge view (Fig. 11). Perturbations with the shorter 3.3 km wavelength amplify in the layers representing the lower Paleozoic sandstones, but do not show much more than kinematic amplification higher in the section. In this respect the forms of theoretical folds in the linear-

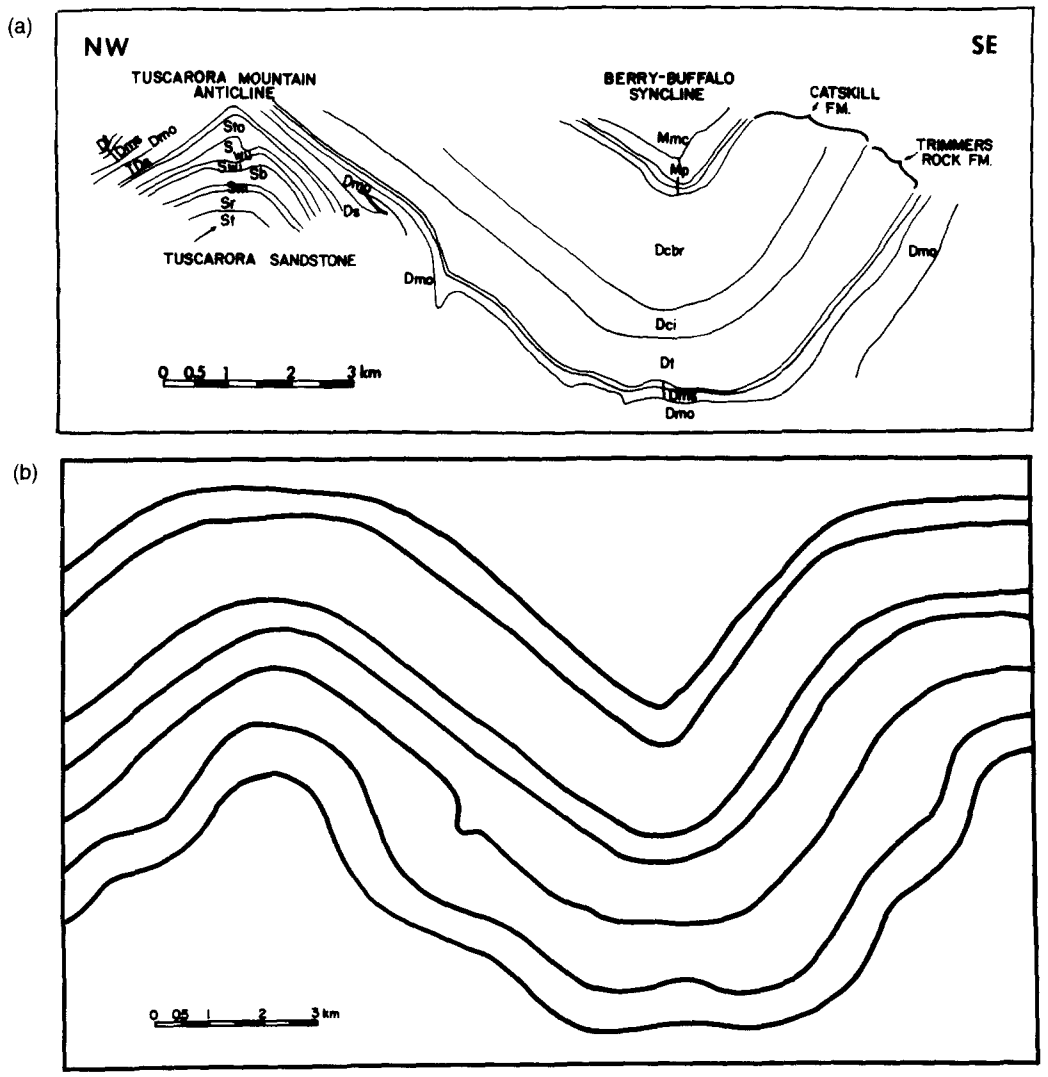

Fig. 11. Form of Berry–Buffalo syncline in Pennsylvania. (a) Down-plunge view. (b) Idealized fold forms from Johnson & Pfaff (1989).

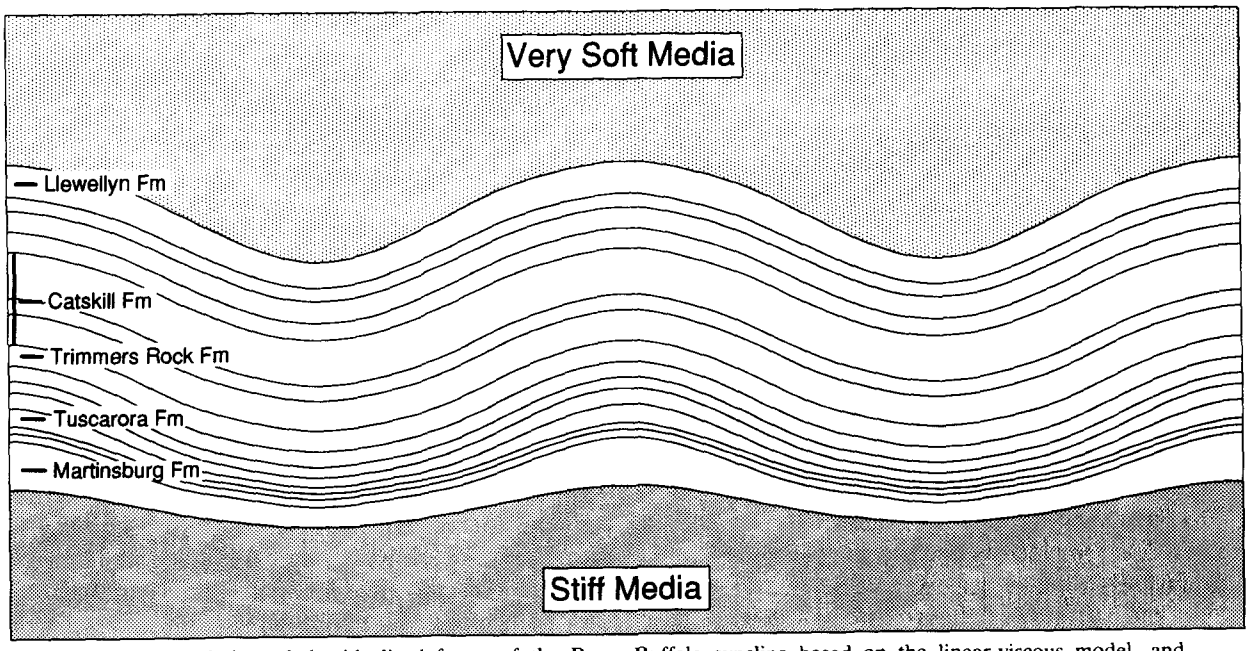

Fig. 12. Simulation of the idealized forms of the Berry–Buffalo syncline based on the linear-viscous model, and structural-lithic units identified in Table 1. The multilayer is confined above by a very soft medium and below by a stiff medium. The initial perturbation was seeded with the first and fifth waveforms. The first waveform amplifies throughout the multilayer. The fifth waveform amplifies very slightly low in the section. Again, the simulation based on linear-viscous fluid satisfactorily models the gross forms of the Berry–Buffalo syncline, but it lacks the sharp form characteristic of the core of the syncline.

viscous model have the same flaw in the multilayer chosen to represent the structural-lithic units in the central Appalachians as they did in the multilayer selected for the 'riverbank exposure' in California. The chevron-like structures of cores of folds is lacking. Thus, some of the elements of the Berry–Buffalo syncline can be seen in the simulation. However the hinges in the simulated folds are more open and rounded than those in the down-plunge view.

SUMMARY AND DISCUSSION

In this paper we have presented a solution for high-amplitude folding of multilayers based on the viscous folding theory developed for single-layers by Fletcher (1974, 1977) and Smith (1975), and for multilayers by Johnson & Pfaff (1989). The maximum amplitude of folds that can be produced with the model depends upon the number of terms used to represent the perturbed flow. Maximum limb slopes of 60–80° can be obtained using the solution technique developed.

We have used the model to reproduce folds in a single layer embedded in less viscous medium (Figs. 4 and 5), and the forms of folds in constrained and unconstrained simple multilayers (Figs. 7 and 8). We have shown that the linear-viscous model reproduces the gross forms of some folds in the Huasna syncline in southern California, and the Berry–Buffalo syncline in Pennsylvania. However, we have shown that even to high-amplitude, the linear-viscous model does not produce the sharpened forms characteristic of chevron-folds and the folds in the Huasna syncline and in the Berry–Buffalo syncline. Presumably we need to analyze folding of non-linear-viscous fluids to have a yield-like behavior to better model chevron folds.

Besides the limitations of rheological behaviors, there are two limitations to the method. First, the simulations presented in this paper require considerable knowledge about the multilayer being simulated. Representing a section as a multilayer requires knowledge of structural-lithic units in a stratigraphic sequence. Each unit in a multilayer must be described in terms of viscosity, thicknesses, and contact properties. This can require detailed field work (e.g. Johnson & Page 1976). After describing the multilayer, the dominant wavelength and eigenvector must be determined (Johnson & Pfaff 1989, Johnson & Fletcher submitted). Determining the dominant wavelength requires considerable computational effort, although programs are available for this (Pfaff 1986, Cruikshank 1991). Once the multilayer has been described mechanically, and the preferred wavelengths calculated, one is ready to proceed with the high-amplitude analysis.

The second limitation of the method, and perhaps the most critical, is the massive computational effort involved in the high-amplitude analysis. The method is numerically intensive. For example, the idealized multilayers in Figs. 7 and 8 have 18 interfaces. Each interface is represented by 161 points, and 10 terms were used in the approximation to the perturbed flow. In evaluating the constants at one stage in the simulation, the matching conditions are evaluated 115,920 times (161 points × 18 interfaces × 10 terms × 4 matching conditions). The result is a 115,920 × 720 matrix, which when squared gives a 720 × 720 matrix to be solved, just to determine the constants which determine the velocities. A Runge–Kutta integration of the velocities to produce displacements requires that in a single increment of deformation the constants are evaluated 4 times—or 463,680 evaluations of matching equations, and four 720 × 720 matrices solved. Over 30 time steps, this requires some 14 million evaluations of matching conditions, and 120 matrix solutions. Also, at each step spline functions representing interfaces must be re-calculated, and some other book-keeping and error-checking performed.

The method can take 1–2 h for one- or two-layer problems when run on a personal computer. Mainframe computers are needed for multilayers. A run can take several days, depending on the computer used. The Berry–Buffalo solutions, using 30 steps, a Runge–Kutta integration, and 10 waveforms can take 6 days of CPU time on a Sun SPARC workstation that is dedicated to running the program. A more detailed discussion of the solution algorithm, and a C-language program are given elsewhere (Cruikshank 1991).

REFERENCES

Anthony, M. & Wickham, J. 1978. Finite-element simulation of asymmetric folding. *Tectonophysics* **47**, 1–14.

Aytuna, S. 1984. Forms of large folds in the central Appalachians, Pennsylvania. Unpublished Ph.D. dissertation, Department of Geology, University of Cincinnati, Cincinnati, Ohio.

Biot, M. A. 1964. Theory of internal buckling of a confined multilayer structure. *Bull. geol. Soc. Am.* **7**, 563–568.

Chapple, W. M. 1970. The finite-amplitude instability in the folding of layered rocks. *Can. J. Earth Sci.* **7**, 475–466.

Chen, R. T. & Oertel, G. 1989. Strain history of the Los Prietos Syncline, Santa Maria Basin, California; a case of post tectonic compaction. *J. Struct. Geol.* **11**, 539–551.

Cruikshank, K. M. 1991. Fracturing in Entrada Sandstone at Arches National Park, Utah, and simulation of high-amplitude folding in viscous multilayers. Unpublished Ph.D. dissertation, Department of Earth and Atmospheric Sciences, Purdue University.

Dahlquist, G. & Björck, Å. 1974. *Numerical Methods*. Prentice-Hall, Englewood Cliffs, New Jersey.

deBremaecker, J.-Cl. & Becker, E. B. 1978. Finite element modeling of folding. *Tectonophysics* **50**, 349–367.

Dieterich, J. H. 1970. Computer experiments on mechanics of finite amplitude folds. *Can. J. Earth Sci.* **7**, 467–476.

Dieterich, J. H. & Carter, N. L. 1969. Stress-history of folding. *Am. J. Sci.* **267**, 129–154.

Dieterich, J. H. & Onat, E. T. 1969. Slow finite deformations of viscous solids. *J. geophys. Res.* **74**, 2081–2088.

Fletcher, R. C. 1967. A finite amplitude model for the emplacement of gneiss domes and salt domes. Unpublished Ph.D. dissertation, Department of Geological Sciences, Brown University.

Fletcher, R. C. 1972. Application of a mathematical model to the emplacement of mantled gneiss domes. *Am. J. Sci.* **272**, 197–216.

Fletcher, R. C. 1974. Wavelength selection in the folding of a single layer with power-law rheology. *Am. J. Sci.* **274**, 1029–1043.

Fletcher, R. C. 1977. Folding of a single viscous layer: Exact infinitesimal-amplitude solution. *Tectonophysics* **39**, 593–606.

Fletcher, R. C. 1991. Three-dimensional folding of an embedded viscous layer in pure shear. *J. Struct. Geol.* **13**, 87–96.

Hudleston, P. J. 1973. An analysis of "single-layer" folds developed experimentally in viscous media. *Tectonophysics* **16**, 189–214.

Hudleston, P. J. & Stephansson, O. 1973. Layer shortening and fold-shape development in the buckling of single layers. *Tectonophysics* **17**, 299–321.

Johnson, A. M. 1977. *Styles of Folding*. Elsevier, New York.

Johnson, A. M. & Fletcher, R. C. Submitted. Theories of folding and density instability. Earth and Atmospheric Sciences Library, Purdue University, West Lafayette, Indiana.

Johnson, A. M. & Page, B. M. 1976. A theory of concentric, kink and sinusoidal folding and of monoclinal flexuring of compressible, elastic multilayers. Part VII, Development of folds within Huasna syncline, San Luis Obispo County, California. *Tectonophysics* **33**, 97–143.

Johnson, A. M. & Pfaff, V. J. 1989. Parallel, similar and constrained folds. *Engng Geol.* **27**, 115–180.

Lan, L. & Wang, R. 1987. Finite-element analysis of an overturned fold using a viscous-fluid model. *Tectonophysics* **139**, 309–314.

Lan, L. & Hudleston, P. J. 1991. Finite-element models of buckle folds in non-linear materials. *Tectonophysics* **199**, 1–12.

Nasir, N. E. & Dabbousi, O. B. 1978. Fluid dynamics model for salt dome evolution. *Tectonophysics* **47**, 85–107.

Nickelsen, R. P. 1963. Fold patterns and continuous deformation mechanisms of the central Pennsylvanian folded Appalachians. In: *Tectonics and Cambrian–Ordovician Stratigraphy in the Central Appalachians of Pennsylvania*. Field Conference sponsored by the Pittsburgh Geological Society and the Appalachian Geological Society, 15–20.

Parrish, D. K., Krivz, A. L. & Carter, N. L. 1976. Finite-element folds of similar geometry. *Tectonophysics* **32**, 183–207.

Pfaff, V. J. 1986. On forms of folds. Unpublished Ph.D. dissertation, Department of Geology, University of Cincinnati, Cincinnati, Ohio.

Pfaff, V. J. & Johnson, A. M. 1989. Opposite senses of fold asymmetry. *Engng Geol.* **27**, 3–38.

Price, N. J. & Cosgrove, J. W. 1990. *Analysis of Geological Structures*. Cambridge University Press, Cambridge.

Sherwin, J. & Chapple, W. M. 1968. Wavelengths of single layer folds: a comparison between theory and observations. *Am. J. Sci.* **266**, 167–179.

Smith, R. B. 1975. Unified theory of the onset of folding, boudinage, and mullion structure. *Bull. geol. Soc. Am.* **86**, 1601–1609.

Smith, R. B. 1979. The folding of a strongly non-Newtonian layer. *Am. J. Sci.* **279**, 272–287.

Stoer, J. & Bulirsch, R. 1980. *Introduction to Numerical Analysis*. Springer, New York.